SIGNATURES OF CORONAL CURRENTS IN MICROWAVE IMAGES

JEONGWOO LEE, STEPHEN M. WHITE, N. GOPALSWAMY and M. R. KUNDU
Department of Astronomy, University of Maryland, College Park, MD 20742, USA

(Accepted: August 12, 1996)

Abstract. Microwave emission from solar active regions at frequencies above 4 GHz is dominated by gyroresonance opacity in strong coronal magnetic fields, which allows us to use radio observations to measure coronal magnetic field strengths. In this paper we demonstrate one powerful consequence of this fact: the ability to identify coronal currents from their signatures in microwave images. Specifically, we compare potential-field (i.e., current–free) extrapolations of photospheric magnetic fields with microwave images and are able to identify regions where the potential extrapolation fails to predict the magnetic field strength required to explain the microwave images. Comparison with photospheric vector magnetic field observations indicates that the location inferred for coronal currents agrees with that implied by the presence of vertical currents in the photosphere. The location, over a neutral line exhibiting strong shear, is also apparently associated with strong heating.

1. Introduction

It has long been recognized that microwave emission from solar active regions offers a unique diagnostic of coronal magnetic fields above active regions. In regions where the microwave radiation is dominated by gyroresonance emission, the total field strength can be determined using the gyroresonant condition $B = \nu/2.8n$, where B is measured in G, ν in MHz, and $n = 2$, 3, or 4 depending on conditions (Zheleznyakov, 1962; Kakinuma and Swarup,1962). When imaging spectroscopy is available, the dominant radiation mechanism and magnetic field strength at each spatial location can be determined directly from the observations (e.g., Gary and Hurford, 1994; see also Gary and Hurford, 1987). Most previous studies have, however, used data from large arrays such as the VLA and the Westerbork Synthesis Radio Telescope which provide high spatial resolution and dynamic range, but at only a limited number of frequencies. With data at well–separated frequencies, it is necessary to fit the data to a priori magnetic field models in order to determine the conditions in the corona (e.g., Alissandrakis, Kundu, and Lantos, 1980).

In such model-based analyses, a popular choice for the starting model has been a potential field extrapolation from a longitudinal magnetogram. This assumes that no currents are present, i.e., $\nabla\times\mathbf{B} = 0$ (see, e.g. Sakurai, 1982). Some studies have found that the field strengths required to explain microwave observations are well predicted by the potential field extrapolation in some parts of active regions (e.g., Schmeltz *et al.*, 1994). There are also other cases where the coronal field strengths predicted by the potential field extrapolation are insufficient to explain the observed microwave images with the assumption of plausible harmonic values and a plausible guess at the unknown height of the radio source. This was the case in the study of Alissandrakis, Kundu, and Lantos (1980). They interpreted their observed radio image at 5 GHz as due to gyroresonant emission at the second and third harmonics, which required coronal field strengths of 600-900 G. These authors could obtain the strong fields in the extrapolation only after introducing a multiplicative correction factor into the magnetogram. The correction factor could be interpreted as the compensation either for possibly underestimated photospheric fields or for the possible presence of currents (i.e. $\nabla \times \mathbf{B} \neq 0$) that were ignored by the potential field extrapolation.

In other works, a linear force-free field (FFF) extrapolation was used to supplement the potential field assumption. This takes into account the presence of currents, but makes the assumption that the ratio α of the vertical current to the vertical magnetic field component is identical throughout the active region. Alissandrakis and Kundu (1984) have shown that active region microwave emission on two different days can be well fitted by linear FFFs with $\alpha = 4.7 \times 10^{-5}$ km^{-1} and -3.7×10^{-5} km^{-1}, respectively. Schmahl *et al.* (1982) could explain the observed morphology of radio images with a linear force-free field (FFF) extrapolation with $\alpha = 4.4 \times 10^{-6}$ km^{-1}, but were not able simultaneously to obtain the required coronal field strength. To explain the inferred field strength of 600 G, even stronger currents with $\alpha \approx 2 \times 10^{-5}$ km^{-1} localized at a particular position were required. Such localization suggests the obvious possibility that α is not spatially uniform. Chiuderi-Drago, Alissandrakis, and Hagyard (1987) determined the value of α taking into account the plausible height of the radio source. In all of these works images at 5 GHz were used. On the other hand Pallavicini *et al.* (1981) used 10.7 GHz data and accordingly the required field strength for gyroresonance at harmonics 2-3 was as high as 1,280-1,910 G. Based on a comparison with a potential field extrapolation these authors also concluded that presence of a current in the corona was required in order to explain the microwave source as observed. At frequencies lower than 4 GHz (e.g., 1.4 GHz), where weaker magnetic field strengths would be relevant, the radiation tends to be dominated by free-free emission (as judged from plasma parameters inferred from coordinated observations in soft X-rays). In such cases the magnetic field strength required to explain the observed polarization of the free–free emission often comes out higher than predicted by the potential field extrapolation (see Schmeltz *et al.*, 1994, for review).

In comparisons of this type, it is widely recognized that the results depend critically on possible errors in the photospheric field measurement (Alissandrakis, Kundu, and Lantos, 1980). Another important uncertainty in most of these comparisons is the height of the radio source, which determines the appropriate level in the surface field extrapolation at which field strengths are compared (e.g., Chiuderi-Drago, Alissandrakis, and Hagyard, 1987). However, when the maximum field strength at any height in the corona is insufficient to explain the observed radio structure this ambiguity is avoided: this argues in favor of using the higher radio frequencies, which probe the strongest field strengths. In this paper we revisit this problem with recent high–quality radio data obtained using the VLA and a vector magnetogram from

Big Bear Solar Observatory (BBSO). Use of the higher frequencies leads to a more critical test of the potential field model, even under more conservative choices for other parameters. Finally we will make use of a vector magnetogram in order to compare the locations of inferred coronal currents with the observed locations of photospheric currents.

2. Observational Data

The target of our observation was AR 6615 located at S07W30 on 1991 May 7. Figure 1(a) shows a white light image of this active region obtained at BBSO. The active region consists of, at least, six closely-spaced spots as well as many tiny spots all located within a common penumbra. Such a close concentration of strong magnetic flux in the photosphere acts to inhibit the expansion of flux tubes as they rise into the corona and is thus ideal for producing strong magnetic fields in the corona. The magnetogram indicates that the three northernmost spots (labeled S1-S3) are negative polarity while the other three spots (labeled S4-S6) are of positive polarity. The longitudinal magnetogram (obtained at BBSO and calibrated following Varsik's (1995) formula) shows that spots S1 and S4 are strongest in the negative and the positive polarity, respectively, reaching ±1800 G. The magnetic neutral line runs roughly east–west through the active region, but dips southwards just east of S5 after passing between the closely–spaced spots S2 and S5.

The radio observation was made with the VLA in D configuration over 6 hours from 14 UT to 20 UT. Maps were made separately in the left (L) and right (R) circular polarizations. In Figure 1(b)-(d) we show contours of the total intensity ($(R+L)/2$) at 4.9 GHz, 8.4 GHz, and 15 GHz, respectively, overlaid on either a white light image or a longitudinal magnetogram obtained at BBSO. As expected from the concentration of spots, this region was highly unusual in showing at least 4 separate gyroresonance sources at 15 GHz: the brightness of these features allowed us to use self–calibration to improve the dynamic range considerably. In addition, we used a maximum entropy technique to carry out deconvolution. This technique prefers to produce smooth images, but enhances the spatial resolution in regions of the image where the signal–to–noise is high (i.e., the effective spatial resolution varies across the image). In order to exploit the regions of higher resolution, we have convolved the final maps with a restoring beam approximately 40% smaller than would be obtained from a conventional fit to the point–source response. The smoothing nature of maximum entropy deconvolution should ensure that we are not thereby introducing spurious high–resolution structure in regions of low signal–to–noise. After correcting for primary–beam attenuation, the resulting maximum brightness temperatures are $(T_L, T_R) = (5.2, 4.0) \times 10^6$ K at 4.9 GHz (circular $8''$ beam), $(6.3, 4.3) \times 10^6$ K at 8.4 GHz ($5''$ beam) and $(3.4, 1.6) \times 10^6$ K at 15 GHz ($2.5''$ beam). Map noise levels in these high–spatial resolution images were somewhat higher than they would have been with a conventional restoring beam size: in brightness

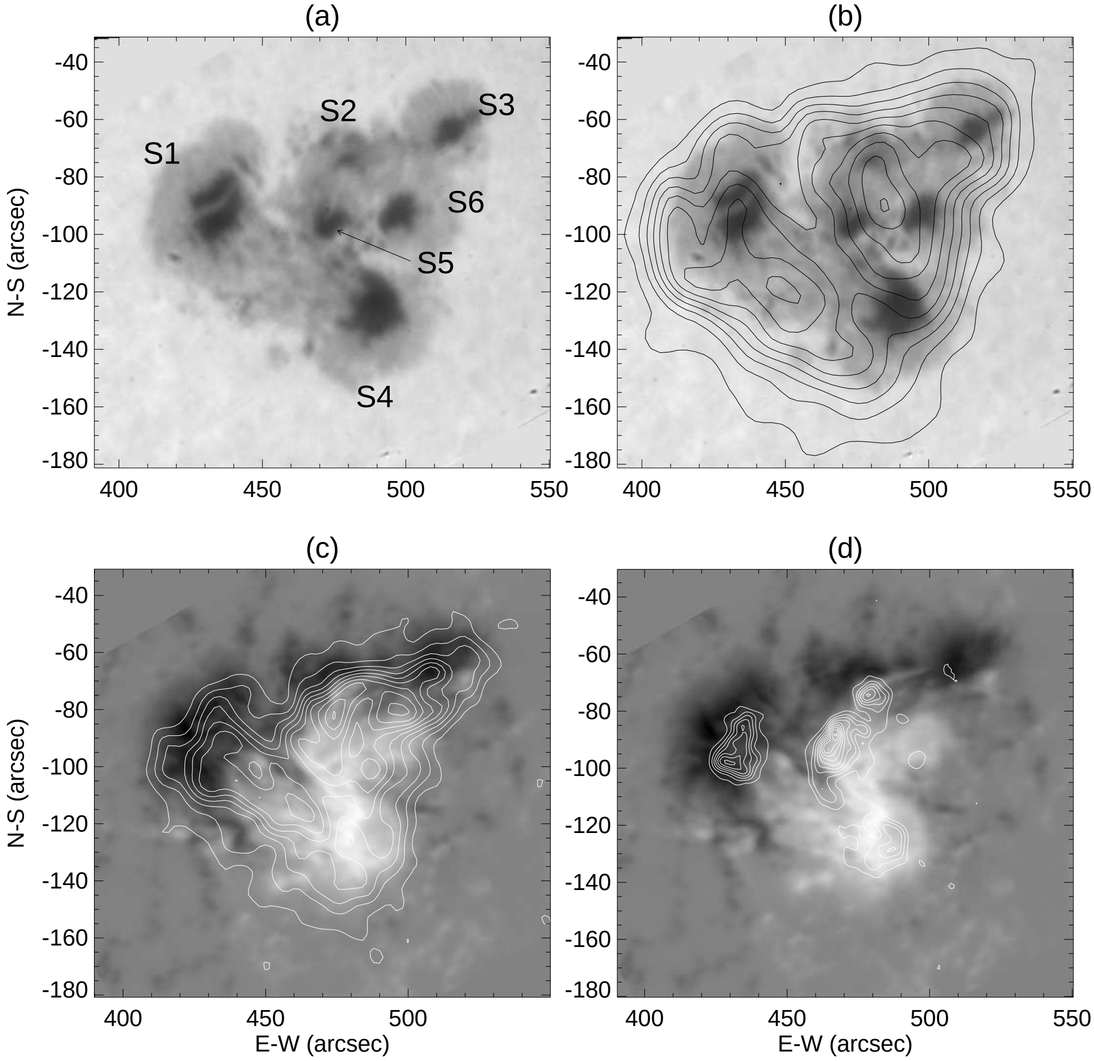

Figure 1. (a) A white light picture of AR6615 obtained at BBSO. (b) Total intensity contours at 4.9 GHz overlaid on the white light picture. Total intensity contours at (c) 8.4 GHz and (d) 15 GHz overlaid on the longitudinal magnetogram. The maximum intensities are 4.4×10^6 K at 4.9 GHz, 4.6×10^6 K at 8.4 GHz, and 1.8×10^6 at 15 GHz. Contours begin at 10% of the maximum intensity and then are 10% apart.

temperature they were of order $(61, 26) \times 10^3$, $(160, 89) \times 10^3$, and $(83, 70) \times 10^3$ K at 4.9, 8.4 and 15 GHz, respectively. Each contour in Fig. 1 starts from the 10% level of the maximum brightness temperature and increases by 10% at the next contour. The maximum brightness temperature is 4.6×10^6 K at 8.4 GHz and 1.8×10^6 K at 15 GHz. At 15 GHz the southernmost radio source (over S4) is right circularly polarized while the other sources are left circularly polarized. Degrees of polarization are high: in excess of 70% in the 15 GHz source lying over the neutral line between S2 and S5. At both 4.9 and 8.4 GHz the large source is left circularly polarized, and at 4.9 GHz the degree of polarization decreases monotonically from north to south across the active region.

In this paper we focus on the influence of coronal currents on the coronal magnetic field strengths and therefore the microwave images. Thus we primarily concern ourselves with the size and position of the microwave sources relative to the photospheric magnetic fields. We do not address the details of the radio intensity distribution which depends more strongly on plasma parameters (density and temperature) than on magnetic fields. For our purpose, two things must be established before we can proceed to a quantitative interpretation of the microwave data. One is the dominant radiation mechanism and the other is the effective harmonic, i.e. the highest gyroresonant harmonic which is optically thick. Typically the opacity drops by a factor of order 100 for each increase in the harmonic number and thus any optically–thin gyroresonant layers can safely be ignored. Calculations of the opacity of free–free emission based on soft X–ray observations show that the soft X–ray loops are unlikely to be optically thick at frequencies above 4 GHz, and consequently in the present case, as in all other cases where coronal brightness temperatures have been observed at 5 GHz, the dominant radiation mechanism is likely to be gyroresonant emission. The high degrees of polarization and the decrease in size of the radio source as frequency increases, evident in Figure 1, are consistent with gyroresonant opacity from isogauss layers whose size diminishes as field strength increases.

For typical coronal densities (10^{10} cm^{-3}) and magnetic scale heights, the highest optically thick gyroresonant harmonic is usually inferred to be $n = 3$ for the x mode and $n = 2$ for the o mode, at $T \sim 2 \times 10^6$ K (see, e.g., Alissandrakis, Kundu, and Lantos, 1980). However in this region we infer brightness temperatures as high as 6×10^6 K, and since gyroresonant opacity increases with temperature (see, e.g., Zlotnik, 1968) the $n = 4$ harmonic could be optically thick in the x mode at this temperature. If the electron temperature is 5.5×10^6 K at 8.4 GHz, the full expression for the gyroresonant opacity in the x-mode (Zlotnik, 1968) yields the opacities $\tau(n = 3) \approx 520$, $\tau(n = 4) \approx 4.1$, and $\tau(n = 5) \approx 0.042$ for typical values of the other parameters: $n_e = 10^{10}$ cm^{-3}, $L_B = 10^4$ km, and $\theta = 60°$. While this is no proof that the fourth harmonic should prevail all over the active region, it suggests that the fourth harmonic may be important and further that it be regarded as the maximum possible effective harmonic for this radio source.

Under this assumption a radio emission feature seen at position (x, y) on the 4.9 GHz map is regarded as evidence for the existence of 430 G at the point (x, y, z) where z is a level along the line of sight, but above the coronal base, say $z = h$. Since solar magnetic fields will decrease with height, the existence of 430 G at $z \geq h$ should mean that the field strength at the coronal base $B(x, y, h)$ should be equal to or greater than 430 G. The same argument can be made for 8.4 GHz and 15 GHz, and so we set the following criteria for testing the potential field extrapolation model: (1) $B \geq 430$ G in the coronal regions where 4.9 GHz emission is observed,

(2) $B \geq 750$ G in the 8.4 GHz emission region, and (3) $B \geq 1,330$ G in the 15 GHz emission region. We emphasize that since we are assuming 4th harmonic emission rather than 3rd as in previous studies, these criteria are very conservative.

3. Comparison of Microwave Images with the Potential Magnetic Fields

In this section we perform the potential field extrapolation from magnetograms and compare the results with the coronal field strengths derived above.

We use the original longitudinal magnetogram obtained at BBSO as a minimum boundary condition, in the sense that the magnetogram may underestimate the photospheric fields from region to region due to errors. In the Appendix we estimate the possible effects of both stray light and saturation on the magnetic field strengths. The presence of stray light could lead to underestimation of the longitudinal fields by a maximum of 20%, uniformly over the whole active region. Near spot centers where saturation may occur, we find the underestimation of the field strength to be at most an additional 38%. To allow for these possible errors we have created a modified magnetogram which is enhanced from the original magnetogram by a factor of 1.2 over the whole active region and, in addition, by a factor of 1.66 at the centers of the largest sunspots, S1 and S4. This saturation correction joins to the uniform background enhancement through a Gaussian with FWHM equal to the umbral size. Since the coronal height is another factor which may influence the size of the coronal isogauss surface, we also consider two possible heights for the base of the corona, $h_1 = 4400$ km ($6''$) and $h_2 = 2900$ km ($4''$).

The potential field extrapolation from these two magnetograms into the corona has been performed using the Sakurai code (Sakurai, 1982) and about 1300 field lines are computed. From this result we create a 3-D array of magnetic fields on a uniform grid in (x, y, z) to determine the locations of the gyroresonant layers at three observing frequencies. These results are presented in Figures 2–4. On the left panels of these figures, we plot field lines selected to lie close to the boundary of the gyroresonant layer at each frequency. The topology of the field lines changes little between extrapolations of the original and the modified magnetograms.On the right panels, we compare the calculated gyroresonant layers (white contours) with the observed radio images (grey scale).

3.1. The 4.9 GHz image

Figure 2 shows the result for 4.9 GHz. The whole active region lies inside the fourth harmonic gyroresonant layer of 4.9 GHz and thus the image at this frequency only tests the field extrapolation at the outer edges of the active region.

The boundary of the predicted gyroresonant layer calculated at h_1 from the original magnetogram (dotted line) is slightly smaller than the observed radio image, but has a nearly identical morphology. When the modified magnetogram is used, the

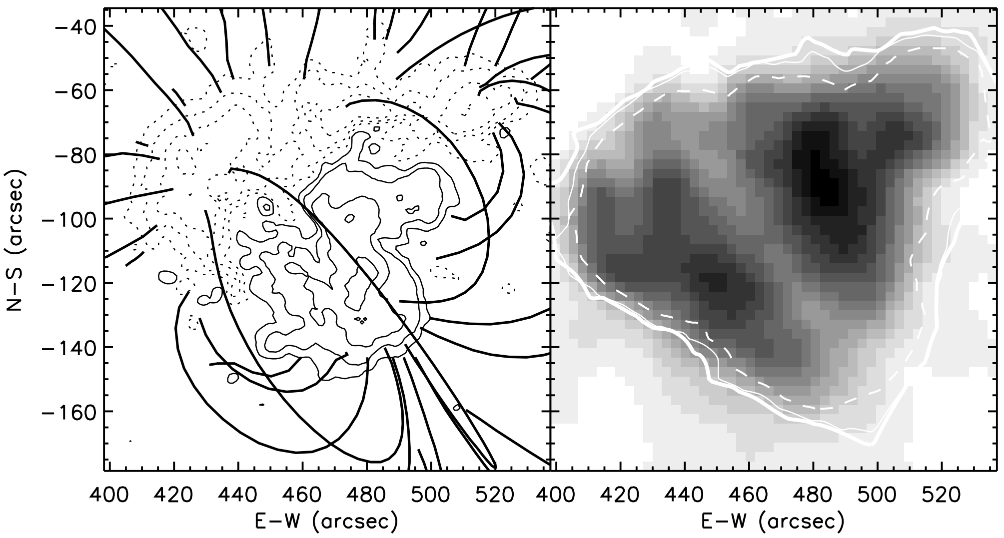

Figure 2. Left panel: magnetic field lines obtained by a potential field extrapolation from the longitudinal magnetogram (contours). Right panel: boundaries of the model $n = 4$ gyroresonant layers at 4.9 GHz. vs. the observed radio image. The radio image is in grey scale with darker features representing brighter radio emission. Solid white lines represent the boundaries of the fourth harmonic gyroresonant layer calculated from the modified magnetogram at two different coronal heights: $h_1 = 4400$ km (thin solid line) and $h_2 = 2900$ km (thick solid lines). The dashed line is the corresponding boundary calculated from the original magnetogram at h_1.

resulting gyroresonant layer (isogauss surface at 340 G) is inflated vertically and the horizontal extent of the isogauss surface increases accordingly (solid lines). Thin and thick solid lines correspond to the assumption of $h = h_1$ and $h = h_2$, respectively. The result is insensitive to the assumption of the coronal height because the isogauss surface at 430 G drops rapidly to the photosphere at its boundary.

A slight extension of the radio source beyond the gyroresonant layer boundary might happen if there is a smooth transition of the dominant radiation mechanism from the gyroemission to free-free emission. At the arcsecond level, scattering of radio waves which is more prominent at lower frequencies (Bastian, 1990) is also a factor which can modify the apparent size of the radio emitting region without changing the morphology. On balance, we find that the 4.9 GHz image is consistent with the potential field extrapolation.

3.2. The 8.4 GHz image

The result for the 8.4 GHz is shown in Figure 3. At 8.4 GHz, the field strength required is $B \geq 750$ G (Section 2). If comparison is made with the gyroresonant layer computed from the original magnetogram (dotted line) there are two regions deficient of strong coronal fields where the radio image implies they should be present. They are denoted as regions A and B in Figure 3.

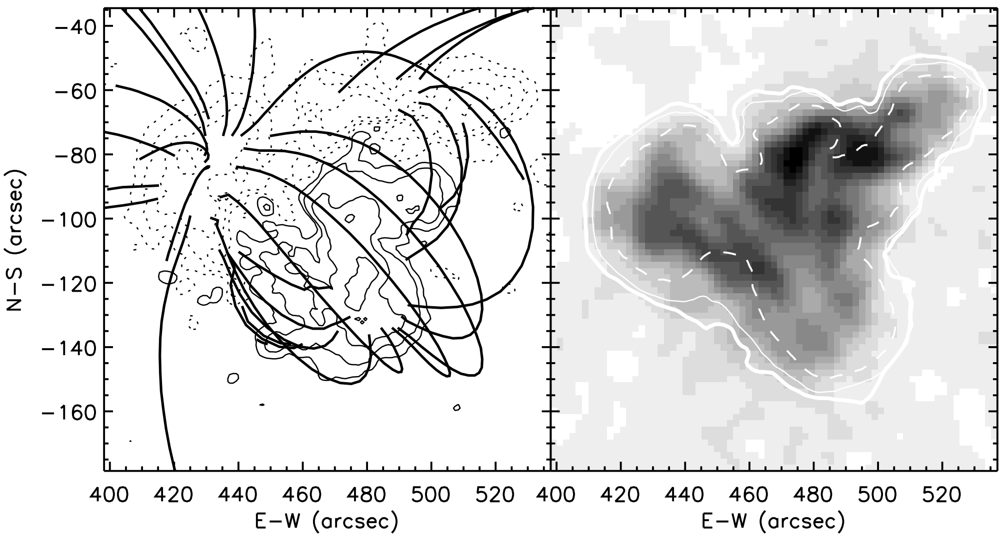

Figure 3. Same as Figure 2 at 8.4 GHz. Arrows indicate the regions deficient of 750 G coronal fields where the radio image implies they should be present.

Region A lies between S2 and S3 in an area where field lines extend high above the surface (see the field line map in Figure 3). After the 20% stay light correction the discrepancy, however, disappears. Region B also lies at an intermediate position between two large spots, S1 and S4, but here the field lines exist as low-lying loops across the magnetic neutral line. In this case, both the stray light correction (thin solid line) and the assumption of a rather low height for the base of the corona, h_2, (thick solid line) lead to an expanded gyroresonant layer large enough to cover the observed image. Therefore again potential fields could be consistent with the 8.4 GHz image if we allow the maximum stray light correction and assume a depressed coronal height.

3.3. The 15 GHz image

Figure 4 shows the result for 15 GHz. At 15 GHz the required field strength is (assuming fourth harmonic) 1330 G (Section 2). Coronal fields this strong are not seen at all at $h \geq h_1$ in the extrapolation of the original magnetogram. When the modified magnetogram is used, however, relatively large coronal regions are found above the large spots S1, S3, and S4 at $h = h_1$ (thin solid line) which satisfy this field strength requirement. In view of the field line map in Figure 4, the 15 GHz sunspot components above S1 and S4 are foot points of a large loop connecting those two spots. The field strength above the small spot S2 never reaches sufficient strength at a height $h = h_1$ to produce 15 GHz gyroresonance emission, but at the lower height $h = h_2$ the potential field model does produce sufficiently strong fields there. S3 lies far from the pointing center of the observation, at about the 25% response level of

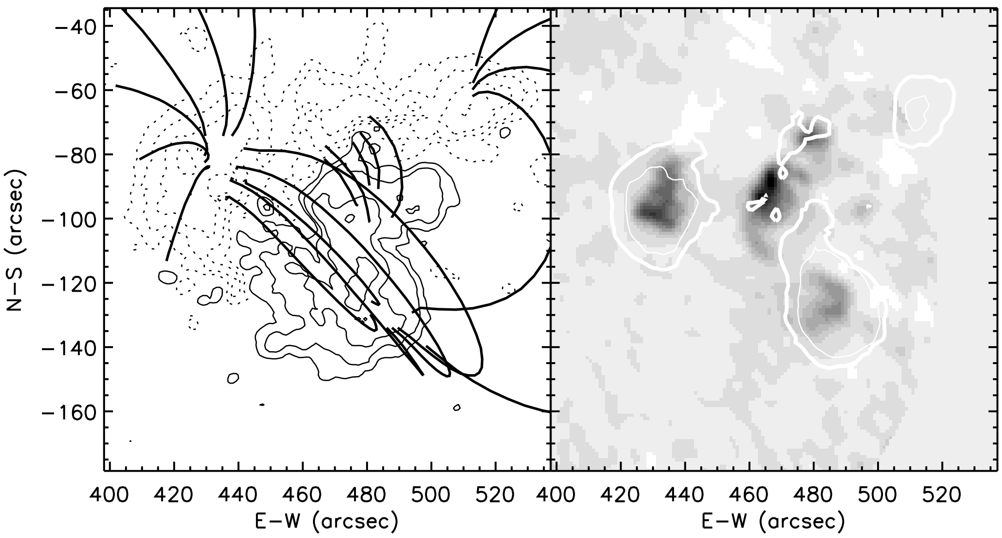

Figure 4. Same as Figure 2 at 15 GHz. The arrow indicates a region deficient of 1330 G coronal fields where the 15 GHz image implies they should be present.

the 15 GHz primary beam. A weak source (L–polarized) is seen over S3, but in view of the large primary–beam correction and the possible effects of beam squint, the true emission level is uncertain and we will not discuss it further here.

However, the central radio component lying above the magnetic neutral line, denoted region C in Figure 4, does not reach sufficient field strength in either magnetogram with either height for the coronal base. The field line map shows that this region contains low lying loops connecting S5 and the southern part of S2. These are stronger loops than those in region B (see Figure 3), having field strengths around 900-1300 G at their top portions, but they do not reach the assumed coronal height, either h_1 or h_2. Since this is a region close to the magnetic neutral line, no stronger saturation or stray light correction would be appropriate. We therefore conclude that this radio source cannot be explained by a potential field extrapolation.

It is true that even this conclusion is somewhat dependent on the assumption regarding the coronal height. If instead, we adopt a height $h \ll h_2$ the discrepancy in this location might vanish, but at the cost of producing larger discrepancies elsewhere in the region. There would also be no reason to believe that the atmosphere above the small spot, S5, should be more depressed than that above the large spots, S1 and S4.

4. The Photospheric Current Structure

The coronal current region identified from the 15 GHz radio images is confined to a local area with dimension comparable to that of the radio image, $\sim 20'' \times 20''$. It is likely, in view of Figure 1, that this coronal current region is connected to S5 and S2 rather than S1. If we tentatively assume that the radio image is tracing the field configuration at the coronal level, we may note that in order for a field line starting from S5 to reach S2 passing through the 15 GHz source it should have rotated by about 30° with respect to the line joining S2 and S4. The rotation of field lines in the presence of a field–aligned current is related to α by $\theta = |\alpha| L/2$ radians (Sakurai, 1979). We thus estimate that $|\alpha| \approx 5 \times 10^{-5}$ km^{-1} for $L \approx 30''$. This quantity is of the same order as previous determinations of α (see Section 1).

In order to simulate the current–carrying field lines in this region, we create a model bipolar sunspot similar to S2 and S4, with one pole at -1500 G and the other at 2000 G, separated by about $30''$, as shown in Figure 5(a), and perform a linear FFF extrapolation using the Fourier-transform method (Alissandrakis, 1980) with $|\alpha|$ as given above. We find that the direction of rotation of the model field lines matches the observed orientation of the radio source when a negative α is used. We thus used $\alpha = -5 \times 10^{-5}$ km^{-1}. Figure 5(b) shows the top-view of the resulting field lines and Figure 5(c) shows the side view. Arrows shown in Figure 5(b) represent transverse magnetic fields at the photosphere ($z = 0$) which we will compare later with the observed vector magnetogram. Dotted lines represent the corresponding results for the potential fields.

The model presented in Figure 5 indicates that the current carrying fields with negative α can successfully explain the 15 GHz image. Firstly, in the presence of currents, the field lines connecting two spots are confined to lower heights (Figure 5(c)) thus maintaining higher field strengths along the field line. By comparison, the potential field lines (dotted lines) are more extended with height and this expansion of the flux tubes leads to reduced field strength at the location of the radio source. Secondly, the rotation pattern of the current carrying field lines with negative α (Figure 5(b)) is consistent with the observed morphology and the apparent location of the radio source to the north-east of S5 (Figure 5(a)). In the potential field model, the source for the 15 GHz image would be an arcade of small magnetic loops crossing the magnetic neutral line which are more or less symmetric. By the projection effect the top portion of this arcade, and therefore the radio source, would lie to the south of the magnetic neutral line, which is above S5. If the loops carried currents in the sense of the positive α, the radio source should have seen to the western side of spot S5, also in contradiction to the observation.

A vector magnetogram carries information on the physical extent and strength of the currents at the photosphere. For instance, under the force-free field assumption the vertical component of the photospheric current, J_z, can be determined as a function of position from the horizontal derivatives of the transverse magnetic fields (see, e.g., Sakurai, 1980). In order to use this technique, however, one must resolve the so-called 180° ambiguity and determine the true directions of the transverse fields. Shown in Figure 6 as arrows are the transverse fields measured at BBSO with orientation determined as follows. In the regions near strong spots S1 and S4 there is no ambiguity since the transverse field appears in radial symmetry. Near the

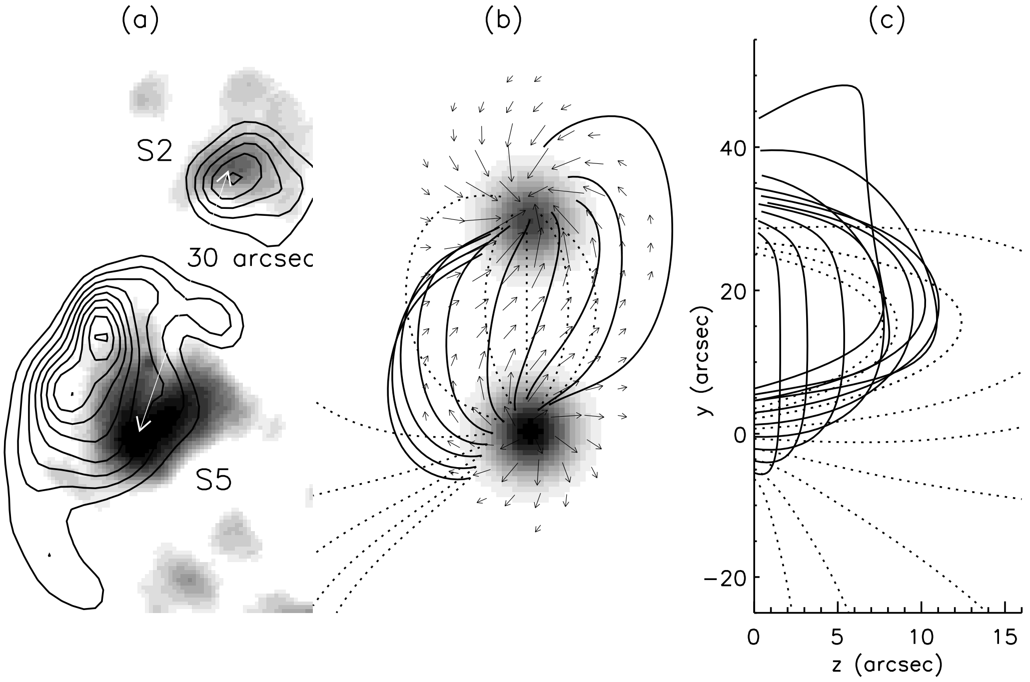

Figure 5. (a) The 15 GHz image shown against the white light picture. The distance between the two spots shown here includes the projection effect. (b) Top view of a linear FFFs from a model bipolar active region. (c) Side view of the model FFFs. Dotted lines are those of the potential fields.

neutral line between S2 and S5, the orientation of the transverse fields is less clear just based on the photospheric fields. However, a careful examination reveals that no alternative choice is possible other than those we display in Figure 6. An ambiguity may arise in the region between S1 and S2 since they all lie in the same magnetic polarity region and no preferred direction exists. At this place we make use of the previous model result, the counterclockwise rotation of the transverse fields around the positive spot (Figure 5), to remove the 180° ambiguity.

On removal of the 180° ambiguity, we use the transverse magnetic fields to calculate the vertical currents J_z at the photosphere. The result is shown in Figure 6 as grey scale images where the currents flowing upward are white and the downward currents are black. Two strong currents regions (J1 and J2 in Figure 6) are found near S2 and S5 which lie symmetric to each other with respect to the neutral line and have opposite directions. We note that the 15 GHz radio source (black contour in Figure 6) lies between J1 and J2. This therefore confirms the connectivity of the current-carrying field lines between the corona and the photosphere, i.e., J1-(the 15 GHz source)-J2. The strength of the photospheric electric current, although subject to large errors, is of order $J_z = -7 \times 10^{-3}$ A m^{-2}, corresponding to $\alpha = -6 \times 10^{-5}$ km^{-1}. Therefore, the sign and the magnitude of the photospheric current as well as

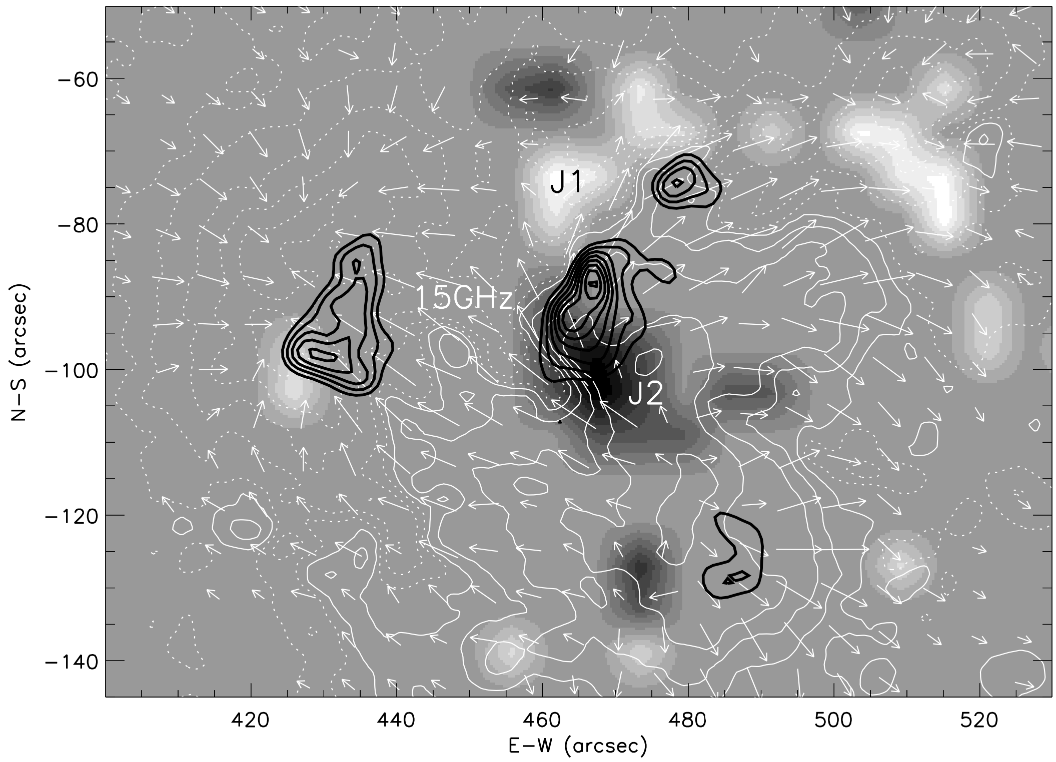

Figure 6. 15 GHz radio images (black contours) vs. the photospheric currents (grey scale). White contours represent the longitudinal fields and white arrows show the transverse fields with the 180° ambiguity removed.

its position are consistent with the interpretation of the coronal currents based on the radio data.

5. Concluding Remarks

In this paper, we have compared the observed radio images of AR6615 using the VLA with predictions of the coronal gyroresonant layers assuming potential fields extrapolated from a BBSO magnetogram. In principle this provides a straightforward technique for identifying coronal currents: one simply compares the locations of the predicted isogauss surfaces (for $n = 4$, these are 430, 750 and 1330 G at 4.9, 8.4 and 15 GHz, respectively) with the observed coronal gyroresonant emission. Where the radio sources are larger than the corresponding predicted isogauss surfaces, currents may be assumed to be inflating the coronal field strength over the values derived in the potential assumption.

However, in practice there are a number of uncertainties which complicate this comparison: (1) errors in the magnetograms, (2) uncertainty regarding the true height above the photosphere at which the corona begins, and (3) the possibility that we are assuming the wrong harmonic number. The first two uncertainties depend on the radio frequency to some extent. At low frequency, the prediction for the horizontal extent of a gyroresonant layer could be insensitive to magnetogram errors and the coronal height assumption. However, the field strength required for gyroresonance at low frequency is also low and provides less of a constraint on the magnetic field model, unless a strong radio source is seen at the boundary. Gyroemission at a high frequency requires strong magnetic fields and makes the test more critical, although the prediction for the gyroresonant layer is sensitive to the errors in the magnetogram and the assumption of the coronal height.

In this study, we have set an upper bound for the magnetogram errors by comparing the intensity and polarization measurement in the present data with the published results for intrinsic values of sunspots (Kopp and Rabin, 1992; Martínez Pillet and Vázquez, 1993). Based on this we did not consider several candidates for coronal current locations which were inferred from the original magnetogram alone. However, the 15 GHz source above a neutral line where a clear deficiency of 1330 G fields is seen in the potential extrapolation, even with the largest possible stray light correction, could not be so dismissed.

The height of the base of the corona above the layer in which the photospheric field is measured remains an uncertainty. In some previous works (e.g., Schmeltz *et al.*, 1994), a coronal height as large as 5,000-10,000 km was used to discriminate the potential field model, which would, however, refer to normal solar atmosphere. On the other hand, empirical models for sunspot atmospheres (Lites and Skumanich, 1981; Yun, Beebe, and Baggett, 1981) predict that the chromosphere above sunspots may be as thin as 1,100 km-2,600 km. Adding 500 km for the photospheric thickness (Vernazza, Avrett and Loeser, 1981) to these results the coronal height lies in the range $h =$1,600 km-3,100 km. Evidence for a low coronal height above active regions is also found in microwave observations by Shibasaki et al. (1983) who deduced the height of microwave sources over a large spot to be less then 3,000 km. Aschwanden *et al.* (1995) determined the height from stereographic observation of gyroemission to be 2,600 km. Our conclusion for the non-potential coronal fields was made based on the assumption $h = 2,900$ km which is in overall agreement with these considerations.

We note that uncertainty (3) includes the possibility that there is a nonthermal electron population present: this does not change the fact that gyroemission is appropriate, but may increase the relevant harmonic. In theory, creation of the nonthermal electrons, as well as that of hot thermal electrons, could be one of the possible consequences of the presence of currents in the corona (cf. Chiuderi-Drago, Alissandrakis, and Hagyard, 1987). The observed high brightness temperature at 15 GHz in this region is consistent with both hypotheses. However, if nonthermal electrons are present, our assumption of fourth harmonic emission may be incorrect. We believe that nonthermal electrons are not present based partly on previous VLA observations which have not indicated their presence (although they have been inferred occasionally from observations with other telescopes, e.g., Akhmedov *et al.* 1986; Chiuderi-Drago, Alissandrakis, and Hagyard, 1987), and also on the polarization of the 15 GHz source associated with the current: it requires less special circumstances to produce the observed high degree of polarization (up to 80%) with a thermal source than with a nonthermal source.

While our identification of the 15 GHz source with a coronal current region was solely based on the magnetic field strength argument (see Section 2), further support for the conclusion has been gathered in examining the morphology of the 15 GHz source in terms of a linear FFF model. Namely, the detailed morphological properties of the 15 GHz source are reproduced by the FFF model with a particular sign and value of α. This information was deduced only from the radio data and the longitudinal magnetogram, and confirmed later by analysis of the vector magnetogram. It is true that analysis of a vector magnetogram can yield information of currents at the photospheric level and allows conjecture of its 3-D structure. However the analysis of vector magnetic fields is subject to noise in the magnetogram and the 180° ambiguity. Therefore, it will be advantageous to have additional diagnostics for currents at a height other than the photosphere to confirm such conjectures.

How widely applicable are the diagnostics presented in this paper? As indicated above, errors in the photospheric magnetograms are a major source of uncertainty in this comparison, and so it is important to have the best possible vector magnetic field data. Due to both saturation and the depressed atmosphere right above umbrae, sunspots may not be the best place to use this diagnostic. As in this example, neutral lines showing sheared fields are good targets for this purpose because they are free of saturation effects from which high resolution magnetograms often suffer. In this case a high spatial resolution magnetogram can be more suitable for exploring detailed magnetic properties in such regions. The manetic fields above neutral lines are also theoretically interesting objects since dynamical interaction with surrounding material is expected to play a role in the resulting structure and field strengths (cf. Low, 1993).

Finally we note that in this study we have ignored much of the information contained in the radio images in order to focus on the presence of coronal currents as reflected by the outer boundaries of the gyroresonance layers. The maps contain intensity and polarization structures which can also be used to investigate the plasma distribution in the corona over the active region. This work is underway and will be presented elsewhere.

Acknowledgements

In many parts of the present work we have benefited from the help of others. We thank R. Fear for providing the BBSO data. We thank Dr J. Varsik and Prof H. Wang for their help in calibrating the vector magnetogram. We thank Prof H. S. Yun for discussions on sunspot atmospheric models. In particular we have greatly benefited from discussions with Dr J.-C. Chae on the stray light effect and Dr A. N. McClymont on coronal loop heights. We also appreciate helpful comments from Prof T. Sakurai and Dr T. Amari on field extrapolation techniques. This work has been supported by NSF grant ATM–93–16972 and NASA grant NAG–W–1541.

Appendix

Here we briefly outline our argument for the extent of underestimation of the photospheric magnetic fields in the present magnetogram.

Underestimation of the longitudinal magnetic fields may happen due to either saturation of the magnetogram or the stray light effect. The stray light effect consists of seeing and scattering. The former is important in measurement of small scale fields such as the network elements (Lee *et al.*, 1996) while the latter is more important in measurement of large scale magnetic feature like the active region (Chae, 1996).

To estimate the amount of scattering we first consider the observed contrast of sunspot intensity (Figure 1(a)) since it is free of saturation. We let ϵ represent the fraction of the scattered light in the total incident light. The observed intensity in a spot can then be written as $I^{obs} = (1-\epsilon)I + \epsilon S$ where I is the intensity inside the spot and S is intensity in the background photosphere. The first term in RHS represents loss of original signal by being scattered out from the source and the second term, the contribution from outside the source by the scattering. If we use the normalized intensity I/S instead of I, the above expression is simplified to $I^{obs} = (1-\epsilon)I + \epsilon$.

From Figure 1(a) we measure $I^{obs} \sim 0.28$ at spots S1 and S3. We tentatively assume that this low contrast is due to the effect of degradation under stray light, which should otherwise be as good as $I \sim$ 0.06-0.10 for spots with umbral diameter, 20-25 arcsec (Matínz Pillet and Vázquez, 1993, their Figure 12). The amount of the stray light must be $\epsilon \approx$ 0.17-0.20 to account for I^{obs}. ϵ is determined by conditions in the Earth's atmosphere and by the instrument and is not a position-dependent quantity. The range for ϵ here is due to uncertainty in the correlation between umbral size and intrinsic field strength. We thus set $\epsilon = 0.2$ as an upper limit to the real ϵ.

To accommodate the spatial variation of field underestimation, we consider a correction factor for the magnetogram, $a(r) = (V^{obs}/V) \times (I^{obs}/I)^{-1}$, as a function of distance r. The expression for (I^{obs}/I) is already obtained above. The corresponding expression for V can be as simple as $(V^{obs}/V) = (1-\epsilon)$ because there is no significant source of polarization available from outside of a spot and a spot only loses its polarized light by the fraction, ϵ. Therefore, the underestimation factor is $a(r) = [I^{obs}(r) - \epsilon]/I^{obs}(r)$. This means that over most of the image except near the spot center where I^{obs} is much smaller than unity, the underestimation due to the stray light effect should be a slowly varying function of distance with the value given approximately by $a(r) \approx 1 - \epsilon$.

At the spot core the underestimation factor should decrease further because not only the scattering effect increases but also the magnetogram suffers the saturation effect. Since there is no simple way to separate these two effects, we simply estimate $a(r = 0)$ from direct comparison of the measured V/I with the intrinsic values published. From Figure 5 of Kopp and Rabin (1992), we find $B \approx 3,000 - 3,200$ G for spots with diameter, $d \approx$ 20-25 arcsec. Assuming that these correspond to intrinsic field strengths of the spots S1 and S4, we presume that the field strength measured in the magnetogram amounts to only 60% of its intrinsic value. To sum up, $a(r = 0) \approx 0.6$ and $a(r > d/2) \approx 0.8$.

References

Akhmedov, Sh. B., & 8 others: 1986, *Astrophys. J.* **301**, 460.
Alissandrakis, C. E.: 1981, *Astron. Astrophys.* **100**, 197.
Alissandrakis, C. E., Kundu, M. R., and Lantos, P.: 1980, *Astron. Astrophys.* **82**, 30.
Alissandrakis, C. E. and Kundu, M. R.: 1984, *Astron. Astrophys.* **139**, 271.
Aschwanden, M. J., Lim, J., Gary, D. E., Klimchuk, J. A.: 1995, *Astrophys. J.* **454**, 512.
Bastian, T. S.: 1990, *Solar Phys.* **130**, 265.
Chae, J.-C.: 1996, Ph D thesis, Seoul National University.
Chiuderi-Drago, F., Alissandrakis, C., and Hagyard, M.: 1987, *Solar Phys.* **112**, 89.
Gary, D. E. and Hurford, G. J.: 1994, *Astrophys. J.* **420**, 903.
Gary, D. E. and Hurford, G. J.: 1987, *Astrophys. J.* **317**, 522.
Kakinuma, T. and Swarup, G.: 1962, *Astrophys. J.* **136**, 975.
Kopp, G. and Rabin, D.: 1992, *Solar Phys.* **141**, 253.
Lee, J., Chae, J.-C., Yun, H. S., and Zirin, H.: 1996, in preparation.
Lites, B. W. and Skumanich, A.: 1981, in Lawrance E. Cram and John H. Thomas, (eds.) *The Physics of Sunspots*, Sacramento Peak Observatory, p.156.
Low, B. C.: 1992, *Astrophys. J.* **399**, 300.
Martínez Pillet, V. and Vázquez, M.: 1993, *Astron. Astrophys.* **270**, 494.
Pallavicini, R., Sakurai, T., and Vaiana, G. S.: 1981, *Astron. Astrophys.* **98**, 316.
Sakurai, T.: 1982, *Solar Phys.* **76**, 301.
Sakurai, T.: 1980, *Solar Phys.* **69**, 343.
Sakurai, T.: 1979, *Publ. Astron. Soc. Japan* **31**, 209.
Schmahl, E. J., Kundu, M. R., Strong, K. T., Bentley, R. D., Smith, J. B., and Krall, J. R.: 1982, *Solar Phys.* **80**, 233.
Schmelz, J. T., Holman, G. D., Brosius, J. W., and Wilson, R. F.: 1994, *Astrophys. J.* **434**, 786.
Shibasaki, K., Chiuderi Drago, F., Melozzi, M. Slottje, C., and Antonucci, E.: 1983, *Solar Phys.* **89**, 307.
Varsik, J. R.: 1995, *Solar Phys.* **161**, 207.
Vernazza, J., Avrett, H., and Loeser, R.: 1981, *Astrophys. J. Suppl.* **45**, 635.
Yun, H. S., Beebe, H. A., and Baggett, W. E.: 1981, Lawrance E. Cram and John H. Thomas, (eds.), *The Physics of Sunspots*, Sacramento Peak Observatory, p.148.
Zheleznyakov, V. V.: 1962, *Astron. Zh.* **39**, 5 (*Soviet Astron.* **6**, 3).
Zlotnik, E. Ya.: 1968, *Astron. Zh.* **45**, 310 (*Soviet Astron.* **12**, 245).